Ultrahigh Resolution Wide Swath MIMO-SAR

Ultrahigh Resolution Wide Swath MIMO-SAR

Mohammed AlShaya, *Graduate Student Member, IEEE*, Mehrdad Yaghoobi, *Member, IEEE*, and Bernard Mulgrew, *Fellow, IEEE*

***Abstract*—A new multiple-input multiple-output (MIMO) synthetic aperture radar (SAR) configuration using multiple contiguous azimuth beams is proposed to map wider image swaths with higher cross-range resolution as compared with the conventional MIMO-SAR. The proposed configuration is independent of the orthogonal waveforms used for transmission and it allows the use of all the phase centers including the overlapping ones to reduce the minimum operating pulse repetition frequency that should be satisfied to avoid aliasing in the azimuth dimension unlike the case of the conventional MIMO-SAR in which only the nonoverlapped phase centers and one of each overlapped phase centers are utilized. This is the result of employing multiple contiguous azimuth beams which makes the echoes, whose effective phase centers are overlapped, occupy different Doppler bandwidths. Each transmitted waveform consists of a sequence of subpulses such that each subpulse is a conventional linear frequency modulated waveform. Echoes corresponding to different phase centers at a given receiver are separated using digital beamforming on receive in elevation. The estimated range profile is free from interrange cell interference as frequency domain system identification-based estimation algorithm is used to identify the impulse response in the range dimension. Finally, both simulated and constructed raw data are used to validate the efficiency of the proposed algorithm.**

***Index Terms*—Multiple-input multiple-output (MIMO), system identification, SAR.**

I. Introduction

THE possibility of imaging a high-resolution wide-swath scene using multiple-input multiple-output (MIMO) synthetic aperture radar (SAR) has been first addressed in [1] where the contradicting requirements of having the desired swath width and high cross-range resolution in conventional single-input single-output (SISO) SAR are mitigated [2]– [4]. MIMO SAR has more effective phase centers as compared with the conventional multichannel SAR due to the use of multiple transmitter along with multiple receiving channels, so further improvements can be achieved. MIMO-SAR can be categorized based on the operation schemes [5] into beam-space MIMO-SAR, multiple subband MIMO-SAR, and orthogonal encoding MIMO-SAR which is the one considered in this article.

Beam-space MIMO-SAR [6] is used to obtain high resolution ultrawide swath imaging by illuminating different subswaths by different subapertures in azimuth. The main disadvantage of this mode is the high complexity of the implementation. The waveforms in multiple subband MIMO-SAR occupy different subbands and are emitted at the same time using different carrier frequencies [7]– [9]. The use of subbands increases the transmitted bandwidth significantly and the narrowband assumption is relaxed to the individual transmitted subband. interrange cell interference (IRCI)-free multiple subband MIMO-SAR is proposed in [7] where multiple narrow receiving beams with multiple phase centers are used. This configuration has an advantage that the echoes corresponding to different transmitted subband waveforms are processed simultaneously at the receiver without a need to separate them. This allows to utilize the bandwidth at the maximum efficiency. The main objective of using this mode is to improve the range resolution.

Orthogonal encoding MIMO-SAR should ideally emits multiple waveforms such that they are mutually orthogonal regardless of the time delays and Doppler shifts [10]. This is possible if the waveforms are transmitted with different times and/or different carrier frequencies which is undesirable [11], [10]. A variety of waveforms are proposed in the literature to address the orthogonality challenge in MIMO-SAR waveforms [12]–[16]. Time-division multiple access waveforms provide a perfect orthogonality but at the expense of a significant loss of the transmit power. In addition, frequency-division multiple access waveforms emit each waveform at different carrier frequency which limits the range resolution to the bandwidth of a single transmitting waveform. Code-division multiple access waveforms can be used but, unfortunately, good autocorrelation and cross-correlation properties cannot be obtained in a single sequence. A class of cyclic prefix based orthogonal frequency division multiplexing waveforms, which is free from IRCI, is proposed in [17] but this kind of waveforms does not fully utilize the transmitted energy as the cyclic prefix is removed at the receiver. In addition, the pulsewidth length is restricted to be at least the same as the channel length to be estimated which is impractical in some applications (i.e., stripmap SAR).

Short-term shift orthogonal waveforms (STSOW) are proposed in [18] in which digital beamforming (DBF) on receive in elevation is employed to separate echoes corresponding to different transmitted waveforms. A class of linear frequency modulated (LFM)-based MIMO waveforms along with DBF in elevation is proposed in [19] in which shifted copies of chirp

Manuscript received February 12, 2020; revised May 22, 2020; accepted September 1, 2020. Date of publication September 4, 2020; date of current version September 18, 2020. The work of Mohammed AlShaya was supported by the King Abdulaziz City for Science and Technology (KACST) in Saudi Arabia. *(Corresponding author: Mohammed AlShaya.)*

Mohammed AlShaya is with the Institute for Digital Communications, University of Edinburgh, EH8 9YL Edinburgh, U.K., and also with the King Abdulaziz City for Science and Technology, Riyadh 12354, Saudi Arabia (e-mail: mohammed.alshaya@ed.ac.uk, malshaya@kacst.edu.sa).

Mehrdad Yaghoobi and Bernard Mulgrew are with the Institute for Digital Communications, University of Edinburgh, EH8 9YL Edinburgh, U.K. (e-mail: m.yaghoobi-vaighan@ed.ac.uk; bernie.mulgrew@ed.ac.uk).

Digital Object Identifier 10.1109/JSTARS.2020.3021914

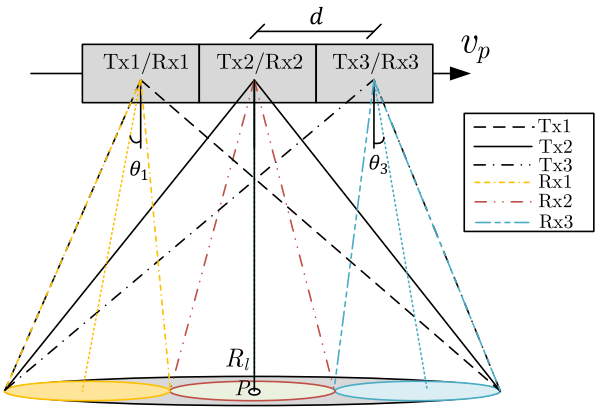

Fig. 1. MIMO-SAR configuration. The wide transmit beams are synthesized from the narrow beams as described in Fig. 2. Each receiver consists of N_{el} elevation channels.

waveforms that share the same carrier frequency and cover the same bandwidth are used. Echoes due to different transmitted waveforms are separated at the receiver using DBF on receive in elevation and null-steering technique. According to the literature [10], the minimum pulse repetition frequency (PRF) in MIMO SAR should satisfy the inequality PRF $\geq B_d/K_p$ where B_d denotes the Doppler bandwidth and K_p is the number of independent phase centers which is, for the case that the same antenna arrays are used for transmission and reception, equal to $M+N-1$ where M and N denote the number of transmitters and receivers, respectively.

In this article, we propose a new MIMO SAR configuration shown in Fig. 1, which is independent of the orthogonal waveforms used for transmission, in which multiple contiguous receiving subbeams with different phase centers and squint angles are generated in the azimuth direction and the wide beams of the transmitters are synthesized from the narrow beams as shown in Fig. 2. Without loss of generality, LFM-based MIMO waveforms [19] will be used in which each of the waveforms used for transmission is a sequence of subpulses consisting of conventional LFM waveforms. Echoes corresponding to different effective phase centers (i.e., transmitters) at the receiver are separated using DBF on receive in elevation and null-steering technique. This is possible because echoes corresponding to different transmitted subpulses (i.e., effective phase centers) arrive at each instant of time from different elevation angles. The main advantage of the proposed configuration over the conventional MIMO-SAR is that all of the effective phase centers are utilized (i.e., even the overlapping ones). In other words, the number of independent effective phase centers in the proposed configuration is $(M \times N)$. This is the result of employing multiple contiguous beams, which makes the echoes at the overlapping effective phase centers occupy different Doppler bandwidths. Therefore, the minimum PRF in the proposed configuration should satisfy the inequality PRF $\geq B_d/(M \times N)$ which provides the opportunity to map wider image swaths with higher cross-range resolution as compared with the conventional MIMO SAR.

In addition, a frequency-domain system identification (FDSI)-based algorithm, which is free from IRCI, is used to estimate the channel impulse response in the range dimension which replaces the conventional matched filter (MF) after formulating the received signals as system identification problems. Finally, initial results of the proposed configuration were reported in [20].

Notations. $(.)^T$ and $(.)^H$ denote the transpose operator and hermitian operator, respectively. Matrices are denoted by upper case bold letters (e.g., $\mathbf{A}$) while scalars and vectors are denoted by upper\lower case letters (e.g., a and A) and bold lower case letters (e.g. $\mathbf{a}$), respectively. $\mathcal{C}$ represents the field of complex numbers. In addition, diag$(\mathbf{a})$ denotes a matrix with vector $\mathbf{a}$ as main diagonal.

II. MIMO-SAR System Model

It is assumed in the derivation of the received signal model that the MIMO-SAR system has M transmit antennas, N receive antennas and N_{el} elevation channels. The received signal at the ith elevation channel in the nth receiving azimuth aperture in the baseband, under the assumption that MIMO-SAR system is narrowband, can be expressed as the following:

$$y_{n,i}(t,\eta) = \sum_{m=1}^{M}\sum_{l=0}^{L-1}\Big(\sigma_l e^{-j2\pi F_c \tau_{l,mn}(\eta)} a_i(\phi_l) \; x(t-\tau_{l,mn}(\eta) - \mid n-m \mid t_d)\Big) + w_{n,i}(t) \quad (1)$$

where,

$$a_i(\phi_l) = e^{j2\pi i d_{\text{el}} \sin(\phi_l)/\lambda}, \quad i = 0,1,\ldots,N_{\text{el}}-1 \quad (2)$$

$$\tau_{l,mn}(\eta) = \frac{R_{l,m}(\eta) + R_{l,n}(\eta)}{c} \quad (3)$$

$x(t)$ is a known transmit waveform (i.e., LFM waveform), N_{el} is the number of elevation channels, the fast time is denoted by t, and η is the slow time. F_c denotes the carrier frequency, σ_l is the radar cross-section (RCS) of the lth scattering point, t_d denotes a delay between the transmitted subpulses, which includes the beam switching time (t_{sw}), d_{el} denotes the distance between the elevation channels, ϕ_l is the elevation angle of the lth range cell, λ denotes the wavelength, c is the speed of light, $R_{l,n}$ denotes the slant range between nth transmitter/receiver to the lth scattering point, and $w_{n,i}(t)$ is additive white noise generated by the nth receiver at the ith elevation channel. $R_{l,m}(\eta) + R_{l,n}(\eta)$ can be approximated as the following [7]:

$$R_{l,m}(\eta) + R_{l,n}(\eta) \approx 2R_{l,m}\left(\eta - \frac{\Delta y_{mn}}{2v_p}\right)_{\theta=\theta_n} + \frac{\Delta y_{mn}^2}{4R_l} \quad (4)$$

where Δy_{mn} is the distance between the mth transmitter and the nth receiver.

Consider the system configuration shown in Fig. 1 in which $M = N = 3$. The timing diagram of the transmitting waveforms is as shown in Fig. 2, which can be used to express the received

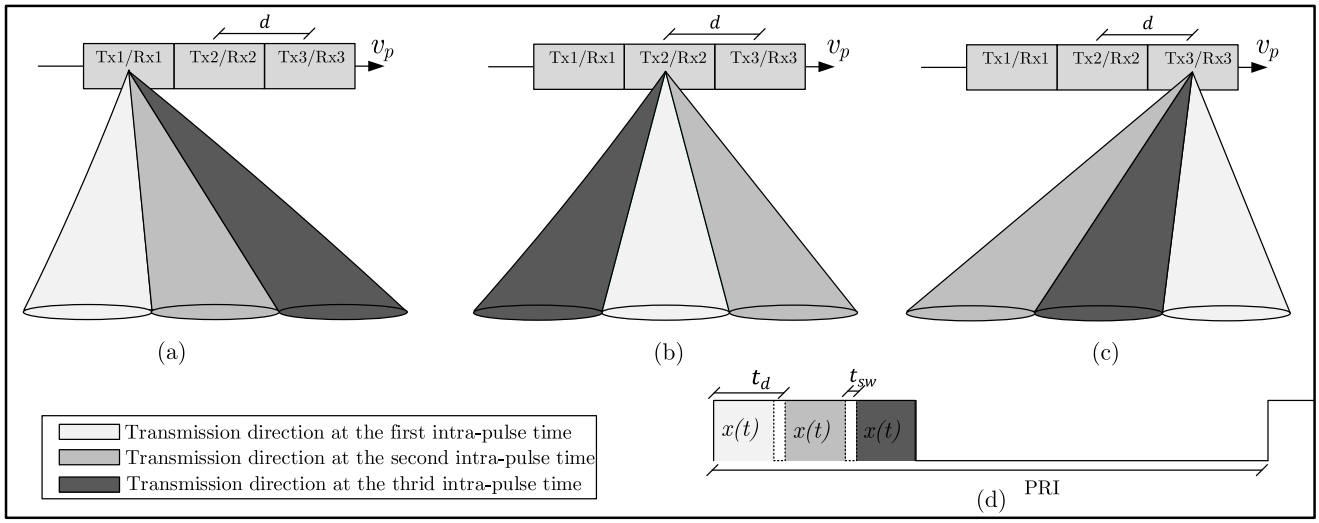

Fig. 2. Wide transmission beams synthesis from narrow beams. (a) Beam directions order of Tx1. (b) Beam directions order of Tx2. (c) Beam directions order of Tx3. (d) Transmitted pulse structure of a PRI transmitted by the mth Tx.

signals at the receivers as the following:

$$y_{1,i}(t,\eta) = \sum_{l=0}^{L-1} \sigma_l e^{-j2\pi F_c \tau_{l,11}(\eta)} a_i(\phi_l) x(t - \tau_{l,11}(\eta)) + \sum_{l=0}^{L-1} \sigma_l e^{-j2\pi F_c \tau_{l,21}(\eta)} a_i(\phi_l) x(t - \tau_{l,21}(\eta) - 2t_d) + \sum_{l=0}^{L-1} \sigma_l e^{-j2\pi F_c \tau_{l,31}(\eta)} a_i(\phi_l) x(t - \tau_{l,31}(\eta) - t_d) + w_{1,i}(t) \tag{5}$$

$$y_{2,i}(t,\eta) = \sum_{l=0}^{L-1} \sigma_l e^{-j2\pi F_c \tau_{l,12}(\eta)} a_i(\phi_l) x(t - \tau_{l,12}(\eta) - t_d) + \sum_{l=0}^{L-1} \sigma_l e^{-j2\pi F_c \tau_{l,22}(\eta)} a_i(\phi_l) x(t - \tau_{l,22}(\eta)) + \sum_{l=0}^{L-1} \sigma_l e^{-j2\pi F_c \tau_{l,32}(\eta)} a_i(\phi_l) x(t - \tau_{l,32}(\eta) - 2t_d) + w_{2,i}(t) \tag{6}$$

$$y_{3,i}(t,\eta) = \sum_{l=0}^{L-1} \sigma_l e^{-j2\pi F_c \tau_{l,13}(\eta)} a_i(\phi_l) x(t - \tau_{l,13}(\eta) - t_d) + \sum_{l=0}^{L-1} \sigma_l e^{-j2\pi F_c \tau_{l,23}(\eta)} a_i(\phi_l) x(t - \tau_{l,23}(\eta) - 2t_d) + \sum_{l=0}^{L-1} \sigma_l e^{-j2\pi F_c \tau_{l,33}(\eta)} a_i(\phi_l) x(t - \tau_{l,33}(\eta)) + w_{3,i}(t). \tag{7}$$

The received signals in (5)–(7) can be expressed as the following after being sampled in both range and azimuth dimensions using the sampling frequencies $f_s = 1/T_s$ and $f_p = \text{PRF}$, respectively. It should be noted that the signal is sampled in the range dimension starting from the near range to the far range.

$$z_{1,i}[n_t, n_a] = \sum_{l=0}^{L-1} \underbrace{(h_{11,i}[l,n_a] + h_{21,i,2d}[l,n_a] + + h_{31,i,d}[l,n_a])}_{h_{1,i}[l,n_a]} x[n_t - l] + w_{1,i}[n_t] \tag{8}$$

$$z_{2,i}[n_t, n_a] = \sum_{l=0}^{L-1} \underbrace{(h_{12,i,d}[l,n_a] + h_{22,i}[l,n_a] + h_{32,i,2d}[l,n_a])}_{h_{2,i}[l,n_a]} x[n_t - l] + w_{2,i}[n_t] \tag{9}$$

$$z_{3,i}[n_t, n_a] = \sum_{l=0}^{L-1} \underbrace{(h_{13,i,d}[l,n_a] + h_{23,i,2d}[l,n_a] + h_{33,i}[l,n_a])}_{h_{3,i}[l,n_a]} x[n_t - l] + w_{3,i}[n_t] \tag{10}$$

where,

$$h_{mn,i}[l,n_a] = \underbrace{\sigma_l e^{-j2\pi F_c \tau_{l,mn}(n_a)}}_{h_{mn}[l,n_a]} a_i(\phi_l) \tag{11}$$

$$h_{mn,i,\alpha d}[l,n_a] = h_{mn,i}[l - \alpha l_d, n_a] \tag{12}$$

$l_d = t_d/T_s$, n_t and n_a denote the range and azimuth time indices, respectively.

III. Azimuth Ambiguity Removal and Image Formation

The received signals are aliased in the azimuth dimension because the azimuth sampling frequency is PRF $= B_d/(MN)$ which is lower than the Doppler bandwidth B_d. It should be borne in mind that the Doppler bandwidth of each of the received

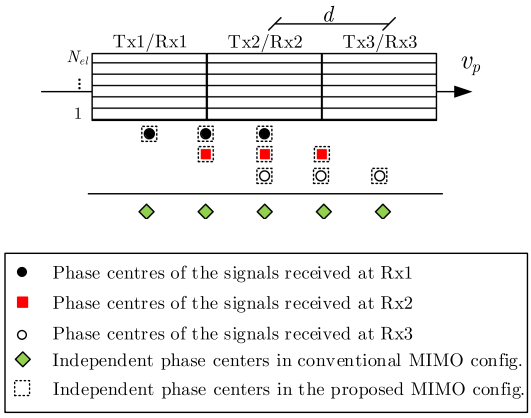

Fig. 3. Locations of the effective phase centers at different receivers. Each group of the phase centers occupies a portion of the total Doppler bandwidth which makes the overlapping phase centers independent (i.e., carries different information).

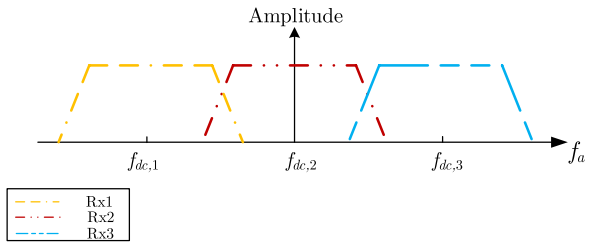

Fig. 4. Spectral distribution of the echo signal in each receiving beam in the proposed MIMO-SAR configuration. $f_{\mathrm{dc},n}$ denotes the Doppler centroid of the echo signal in the nth receiver.

signals expressed in (8)–(10) is B_d/N which corresponds to the receiving beamwidth.

The aliased Doppler spectrum of the signal received at a given receiver can be perfectly reconstructed if there are M independent representations of the aliased signal as stated in the multiaperture reconstruction algorithm [1]. In our proposed configuration, the $M = 3$ independent representations of the impulse response measured from the first receiver are $h_{11,i}$, $h_{21,i}$, and $h_{31,i}$ which can be used to reconstruct the aliased Doppler spectrum that corresponds to the first receiving beamwidth. Similarly, the $M = 3$ independent representations of the impulse response measured from the second and third receivers can be obtained to reconstruct the Doppler spectra of the impulse responses measured from the second and third receivers, respectively. The location of the phase centers that corresponds to different Doppler bandwidth is illustrated in Fig. 3. The phase centers overlapped spatially, in the proposed MIMO-SAR configuration, are independent (i.e., carries different information) because the echoes corresponding to each of the overlapped phase centers occupy a different Doppler bandwidth as shown in Fig. 4 unlike the case of the conventional MIMO-SAR in which the echoes corresponding to all phase centers share the same Doppler bandwidth.

The separation of the impulse responses that correspond to different phase centers can be done by DBF in elevation on receive by exploiting the one to one relationship between time delay and elevation angle in a side-looking radar imaging geometry [21]– [24]. This relation results in that echoes corresponding to different transmitted subpulses (i.e., phase centers) arrive at each instant of time from different elevation angles. Finally, the reconstructed Doppler bandwidth of the receivers should be combined to form the full Doppler bandwidth B_d as explained next.

A. Impulse Response Estimation and DBF in Elevation

The impulse responses $h_{1,i}$, $h_{2,i}$, and $h_{3,i}$ in (8)–(10) will be estimated individually using the FDSI-based estimation algorithm proposed in [7]. It should be noted that each of the impulse responses $h_{1,i}$, $h_{2,i}$, and $h_{3,i}$ occupies a portion of the total Doppler bandwidth. Accordingly, the Doppler bandwidths need to be combined after removing the azimuth ambiguity to form the full Doppler bandwidth.

The received signals in (8)–(10) at the ith elevation channel can be expressed in a matrix form for a given n_a as ($\forall n = 1, 2, 3$)

$$\begin{aligned}\mathbf{z}_{n,i}[n_a] &= [z_{n,i}[0, n_a], z_{n,i}[1, n_a], \ldots, z_{n,i}[K + L - 1, n_a]]^T \\ &= \mathbf{X}\mathbf{h}_{n,i}[n_a] + \mathbf{w}_{n,i}[n_a] \\ &= \mathbf{X}_C \underbrace{\begin{bmatrix}\mathbf{h}_{n,i}[n_a] \\ \mathbf{0}_{(K-1)}\end{bmatrix}}_{\mathbf{h}_{n,i,p}[n_a]} + \mathbf{w}_{n,i}[n_a] \end{aligned} \tag{13}$$

where,

$$\mathbf{X} = \begin{bmatrix} x[0] & 0 & \ldots & \ldots & 0 \\ x[1] & x[0] & & & 0 \\ \vdots & x[1] & \ddots & & \vdots \\ x[K-1] & \vdots & \vdots & \ddots & 0 \\ 0 & x[K-1] & & & x[0] \\ 0 & 0 & \ddots & \vdots & x[1] \\ \vdots & \vdots & & \ddots & \vdots \\ 0 & 0 & \ldots & 0 & x[K-1] \end{bmatrix} \tag{14}$$

The transmitted waveform length is denoted by K and $\mathbf{X}_C$ is the circulant version of $\mathbf{X}$. The estimation of the impulse responses is done by computing the following ($\forall n = 1, 2, 3$):

$$\hat{\mathbf{h}}_{n,i,p}[n_a] = \mathbf{X}_C^{-1}\mathbf{z}_{n,i}[n_a]. \tag{15}$$

The discrete Fourier transform (DFT) decomposition of $\mathbf{X}_C$ expressed below can be utilized to estimate the impulse response, which can be done in the frequency domain.

$$\mathbf{X}_C = \mathbf{F}\mathrm{diag}\{\mathcal{X}\}\mathbf{F}^H \tag{16}$$

where $\mathbf{F}$ denotes the DFT matrix $\mathcal{X}$ is the Fourier transform of the first row of the matrix $\mathbf{X}_C[n_a]$. It should be pointed out that the last $(K - 1)$ elements of the estimated impulse response are replaced by zeroes. The impulse response estimation described abovementioned is performed for all n_a and N_{el}.

The estimated impulse responses for all elevation channels ($\forall i = 0, 1, \ldots, N_{\mathrm{el}} - 1$) at a given range and azimuth bin can

be expressed as the following:

$$\mathbf{h}_1[l,n_a] = [h_{1,0}[l,n_a], h_{1,1}[l,n_a], \ldots, h_{1,(N_{\mathrm{el}}-1)}[l,n_a]]^T = \underbrace{[\mathbf{a}(\phi_l) \quad \mathbf{a}(\phi_{l-2l_d}) \quad \mathbf{a}(\phi_{l-l_d})]}_{\mathbf{A}_1(\phi_l)} \begin{bmatrix} h_{11}[l,n_a] \\ h_{21,2d}[l,n_a] \\ h_{31,d}[l,n_a] \end{bmatrix} \tag{17}$$

$$\mathbf{h}_2[l,n_a] = [h_{2,0}[l,n_a], h_{2,1}[l,n_a], \ldots, h_{2,(N_{\mathrm{el}}-1)}[l,n_a]]^T = \underbrace{[\mathbf{a}(\phi_{l-l_d}) \quad \mathbf{a}(\phi_l) \quad \mathbf{a}(\phi_{l-2l_d})]}_{\mathbf{A}_2(\phi_l)} \begin{bmatrix} h_{12,d}[l,n_a] \\ h_{22}[l,n_a] \\ h_{32,2d}[l,n_a] \end{bmatrix} \tag{18}$$

$$\mathbf{h}_3[l,n_a] = [h_{3,0}[l,n_a], h_{3,1}[l,n_a], \ldots, h_{3,(N_{\mathrm{el}}-1)}[l,n_a]]^T = \underbrace{[\mathbf{a}(\phi_{l-l_d}) \quad \mathbf{a}(\phi_{l-2l_d}) \quad \mathbf{a}(\phi_l)]}_{\mathbf{A}_2(\phi_l)} \begin{bmatrix} h_{13,d}[l,n_a] \\ h_{23,2d}[l,n_a] \\ h_{33}[l,n_a] \end{bmatrix} \tag{19}$$

where,

$$\mathbf{a}(\phi_l) = [a_0(\phi_l), a_1(\phi_l), \ldots, a_{N_{\mathrm{el}}-1}(\phi_l)]^T. \tag{20}$$

The corresponding impulse responses to each transmitter can be separated from $\mathbf{h}_n[l,n_a]$ by multiplying it with the weight matrix $\mathbf{W}_n(\phi_l)$, which can be obtained based on linearly constrained minimum variance beamformer algorithm [25] as the following ($\forall n = 1,2,3$):

$$\mathbf{W}_n(\phi_l) = (\mathbf{A}_n^H(\phi_l)\mathbf{A}_n(\phi_l))^{-1}\mathbf{A}_n^H(\phi_l). \tag{21}$$

The impulse responses are separated for all azimuth and range bins. The delay in $h_{mn,\alpha d}[l,n_a]$ can be easily compensated for in the range frequency domain by multiplying it with $e^{j2\pi f_r \alpha t_d}$ to obtain $h_{mn}[l,n_a]$ where f_r is the range frequency.

B. Azimuth Ambiguity Removal and Image Formation

As described previously, the impulse responses h_{1n}, h_{2n}, and h_{3n} ($\forall n = 1,2,3$) occupy only a portion ($B_d/N = B_d/3$) of the total the Doppler bandwidth, which corresponds to the receiving beamwidth. The Doppler spectra of impulse responses are aliased as the effective sampling frequency in the azimuth dimension is assumed to be ($f_p = \mathrm{PRF} = B_d/(MN) = B_d/9$). The azimuth ambiguity removal of the Doppler spectra that correspond to the first receiving beam (i.e., $n = 1$) will be considered now.

The Fourier transform of h_{11}, h_{21}, and h_{31} across both azimuth and range dimensions can be expressed using the principle of displaced phase center [26] as the following:

$$H_{11}(f_r,f_a) = H_{31}(f_r,f_a)\underbrace{e^{j2\pi d f_a/v_p}e^{j2\pi d^2/(\lambda R_l)}}_{Q_1(f_a)} \tag{22}$$

$$H_{21}(f_r,f_a) = H_{31}(f_r,f_a)\underbrace{e^{j\pi d f_a/v_p}e^{j3\pi d^2/(2\lambda R_l)}}_{Q_2(f_a)} \tag{23}$$

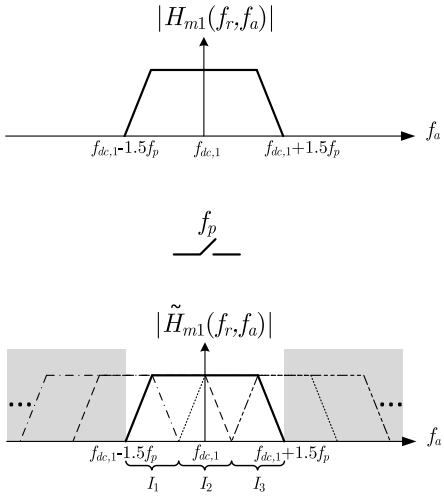

Fig. 5. Spectrum of the impulse response estimated at the first receiver when the transmitted signal is emitted by the mth transmitter before and after sampling with $f_p = \mathrm{PRF}$. $f_{\mathrm{dc},1}$ is the Doppler centroid of the first receiver. The Doppler bandwidth of each receiver is assumed to be 3PRF.

$$H_{31}(f_r,f_a) = H_{31}(f_r,f_a) \times \underbrace{1}_{Q_3(f_a)}. \tag{24}$$

The aliased signals of $H_{m1}(f_r,f_r)$ can be expressed as the following ($\forall m = 1,2,3$):

$$\tilde{H}_{m1}(f_r,f_a) = \sum_{k=-\infty}^{\infty} H_{m1}(f_r,f_a+kf_p) = \sum_{k=-\infty}^{\infty} H_{31}(f_r,f_a+kf_p)Q_m(f_a+kf_p). \tag{25}$$

The aliased Doppler spectrum is divided into M intervals (i.e., $M = 3$) as shown in Fig. 5, namely, I_1, I_2, and I_3 whose center frequencies can be obtained using the following equation:

$$f_{\mathrm{dc},j} = \left(-\frac{M}{2} - 0.5 + j\right)\mathrm{PRF} + f_{\mathrm{dc},n}, \quad \forall j = 1,2,\ldots,M \tag{26}$$

where $f_{\mathrm{dc},n}$ is the Doppler centroid of the nth receiver (i.e., $n = 1$ for the first receiver), which is a function of the squint angle. It is possible for each Doppler interval to weight and combine $\tilde{H}_{11}(f_r,f_a)$, $\tilde{H}_{21}(f_r,f_a)$, and $\tilde{H}_{31}(f_r,f_a)$ in such a way that the original spectrum $H_{31}(f_r,f_a)$ is recovered while the back-folded component is removed as expressed in the following equations for the interval I_1:

$$P_{11}(f_a)\tilde{H}_{11}(f_r,f_a) + P_{21}(f_a)\tilde{H}_{21}(f_r,f_a) + P_{31}(f_a)\tilde{H}_{31}(f_r,f_a) = 3H_{31}(f_r,f_a) \tag{27}$$

$$P_{11}(f_a)\tilde{H}_{11}(f_r,f_a+f_p) + P_{21}(f_a)\tilde{H}_{21}(f_r,f_a+f_p) + P_{31}(f_a)\tilde{H}_{31}(f_r,f_a+f_p) = 0 \tag{28}$$

$$P_{11}(f_a)\tilde{H}_{11}(f_r,f_a+2f_p) + P_{21}(f_a)\tilde{H}_{21}(f_r,f_a+2f_p) + P_{31}(f_a)\tilde{H}_{31}(f_r,f_a+2f_p) = 0. \tag{29}$$

For interval I_2 after shifting to I_1 to allow for setting up the linear systems

$$P_{12}(f_a+f_p)\tilde{H}_{11}(f_r,f_a+f_p)+P_{22}(f_a+f_p)\tilde{H}_{21}(f_r,f_a+f_p)+P_{32}(f_a+f_p)\tilde{H}_{31}(f_r,f_a+f_p)=3H_{31}(f_r,f_a+f_p) \tag{30}$$

$$P_{12}(f_a+f_p)\tilde{H}_{11}(f_r,f_a)+P_{22}(f_a+f_p)\tilde{H}_{21}(f_r,f_a)+P_{32}(f_a+f_p)\tilde{H}_{31}(f_r,f_a)=0 \tag{31}$$

$$P_{12}(f_a+f_p)\tilde{H}_{11}(f_r,f_a+2f_p)+P_{22}(f_a+f_p)\tilde{H}_{21}(f_r,f_a+2f_p)+P_{32}(f_a+f_p)\tilde{H}_{31}(f_r,f_a+2f_p)=0. \tag{32}$$

For interval I_3 after shifting to I_1

$$P_{13}(f_a+2f_p)\tilde{H}_{11}(f_r,f_a+2f_p)+P_{23}(f_a+2f_p)\tilde{H}_{21}(f_r,f_a+2f_p)+P_{33}(f_a+2f_p)\tilde{H}_{31}(f_r,f_a+2f_p)=3H_{31}(f_r,f_a+2f_p) \tag{33}$$

$$P_{13}(f_a+2f_p)\tilde{H}_{11}(f_r,f_a+f_p)+P_{23}(f_a+2f_p)\tilde{H}_{21}(f_r,f_a+f_p)+P_{33}(f_a+2f_p)\tilde{H}_{31}(f_r,f_a+f_p)=0 \tag{34}$$

$$P_{13}(f_a+2f_p)\tilde{H}_{11}(f_r,f_a)+P_{23}(f_a+2f_p)\tilde{H}_{21}(f_r,f_a)+P_{33}(f_a+2f_p)\tilde{H}_{31}(f_r,f_a)=0. \tag{35}$$

The reconstruction filters can be computed as the following:

$$\mathbf{P}(f_a)=3\mathbf{Q}^{-1}(f_a) \tag{36}$$

where,

$$\mathbf{Q}(f_a)=\begin{bmatrix} Q_1(f_a) & Q_2(f_a) & Q_3(f_a) \\ Q_1(f_a+f_p) & Q_2(f_a+f_p) & Q_3(f_a+f_p) \\ Q_1(f_a+2f_p) & Q_2(f_a+2f_p) & Q_3(f_a+2f_p) \end{bmatrix} \tag{37}$$

$$\mathbf{P}(f_a)=\begin{bmatrix} P_{11}(f_a) & P_{12}(f_a+f_p) & P_{13}(f_a+2f_p) \\ P_{21}(f_a) & P_{22}(f_a+f_p) & P_{23}(f_a+2f_p) \\ P_{31}(f_a) & P_{32}(f_a+f_p) & P_{33}(f_a+2f_p) \end{bmatrix} \tag{38}$$

I_1, I_2, and I_3 are then concatenated to obtain the original spectrum $H_{31}(f_r,f_a)$. Similarly, the original spectrum $H_{22}(f_r,f_a)$ is reconstructed using the aliased spectra of $\tilde{H}_{m2}(f_r,f_a)$ and the original spectrum of $H_{12}(f_r,f_a)$ is reconstructed from the aliased spectra of $\tilde{H}_{m3}(f_r,f_a)$ ($\forall m=1,2,3$).

The impulse responses $H_{rx,1}(f_r,f_a)=H_{31}(f_r,f_a)$, $H_{rx,2}(f_r,f_a)=H_{22}(f_r,f_a)$, and $H_{rx,3}(f_r,f_a)=H_{13}(f_r,f_a)$ have the same phase center but each occupies a portion of the total Doppler bandwidth. The Doppler centroids of $H_{rx,1}(f_r,f_a)$, $H_{rx,2}(f_r,f_a)$, and $H_{rx,3}(f_r,f_a)$ are functions of the squint angles θ_1, θ_2, and θ_2, respectively. Without loss of generality, range-Doppler algorithm is used for image formation [27]. The range cell migration correction (RCMC) is performed by multiplying $H_{rx,n}(f_r,f_a)$ by the following ($\forall n=1,2,3$):

$$H_{\text{RCMC},n}(f_r,f_a)=e^{-j2\pi\Delta t_n(r_{\text{ref}},f_{a,n})f_r} \tag{39}$$

where,

$$\Delta t_n(r_{\text{ref}},f_{a,n})=\frac{2}{c}r_{\text{ref}}\left(1-\frac{1}{\sqrt{1-(\frac{\lambda f_{a,n}}{2v_p})^2}}\right) \tag{40}$$

$$\frac{-M\text{PRF}}{2}+f_{\text{dc},n}\le f_{a,n}\le\frac{M\text{PRF}}{2}+f_{\text{dc},n} \tag{41}$$

r_{ref} is a reference range and $f_{\text{dc},n}$ denotes the Doppler centroid of the nth receiver. The full Doppler bandwidth is then synthesized before forming the image by performing the following steps [7].

1) Transform RCMC data of each receiver into range time-Doppler domain.
2) Zero-pad the data in the Doppler dimension such that the number of samples of each Doppler spectrum is increased by a factor of N.
3) Compensate for the Doppler shift introduced by the receiving beams squint angles. This can be done by shifting the data in the Doppler dimension by the corresponding Doppler centroids.
4) Superimpose the data of all receiving beams to obtain the full bandwidth Doppler spectrum.

The data are then multiplied by H_{RD} defined below in the range time-Doppler domain to perform azimuth compression.

$$H_{\text{RD}}(n_t,f_d;r_{\text{ref}})=\exp\left[\frac{j2\pi r_{\text{ref}}}{v_p}\sqrt{f_{am}^2-f_d^2}\right] \tag{42}$$

$$\frac{-NM\text{PRF}}{2}\le f_d\le\frac{NM\text{PRF}}{2} \tag{43}$$

where $f_{am}=2v_p/\lambda$. Finally, the image is formed by calculating the inverse Fourier transform in the azimuth dimension.

C. Azimuth Ambiguity Analysis

In the proposed MIMO-SAR configuration, the receive beams of the channels are very close to each other in azimuth. Accordingly, the sidelobes of the receive beams will overlap with mainlobes of the adjacent azimuth beams, which would degrade the performance of the azimuth ambiguity to signal ratio (AASR).

In this section, the transmit and receive beam patterns are assumed to be raised cosine functions. The one way normalized azimuthal power pattern of the nth azimuth channel can be expressed as follows: ($\forall n=1,2,3,\ldots,N$)

$$G_n(\theta)=\left(\text{sinc}\left(U_n(\theta-\theta_n)\right)\frac{\cos(\pi U_n(\theta-\theta_n))}{1-4(U_n(\theta-\theta_n))^2}\right)^2 \tag{44}$$

where,

$$U_n(\theta)=\frac{\pi L_a\cos(\theta_n)}{\lambda}\sin(\theta) \tag{45}$$

θ_n is the squint angle of the nth receiving beam and L_a denotes the antenna azimuth length of the receiver. The AASR can be expressed as follows:

$$\text{AASR}_n=\frac{P_{n,\text{ambig}}}{P_{n,\text{sig}}} \tag{46}$$

where,

$$P_{n,\text{ambig}} = \sum_{\substack{k=-\infty \\ k\neq 0}}^{\infty} \left[\int_{(f_{\text{dc},n}-0.5B_{d,\text{Rx}})}^{(f_{\text{dc},n}+0.5B_{d,\text{Rx}})} G_n^2(f+kf_r)\mathrm{d}f + \sum_{m\neq n} \int_{(f_{\text{dc},n}-0.5B_{d,\text{Rx}})}^{(f_{\text{dc},n}+0.5B_{d,\text{Rx}})} G_n(f+kf_r)G_m(f+kf_r)\Delta_{nm}\mathrm{d}f \right] \tag{47}$$

$$P_{n,\text{sig}} = \int_{(f_{\text{dc},n}-0.5B_{d,\text{Rx}})}^{(f_{\text{dc},n}+0.5B_{d,\text{Rx}})} G_n^2(f)\mathrm{d}f + \sum_{m\neq n} \int_{(f_{\text{dc},n}-0.5B_{d,\text{Rx}})}^{(f_{\text{dc},n}+0.5B_{d,\text{Rx}})} G_n(f)G_m(f)\Delta_{nm}\mathrm{d}f \tag{48}$$

$B_{d,\text{Rx}}$ denotes the Doppler bandwidth of a single receiver and Δ_{mn} is a factor which is equal to one when the waveforms emitted by all transmitters are the same (i.e., LFM waveform). The azimuth ambiguity in (47) is a sum of two components in which the first one is the same as the SISO SAR and the second component which is a result of the echoes which correspond to the signals emitted by the other beams.

The AASR can be improved when STSOW [11] are used in such a way that when a given transmitter (i.e., Tx1) emits a conventional LFM chirp, the next adjacent transmitter (i.e., TX2) emits the same conventional LFM chirp but with sufficient offset in its instantaneous frequencies. The factor Δ_{mn} in this case can be expressed as follows:

$$\Delta_{mn} = \begin{cases} 0, & x_n \neq x_m \\ 1, & \text{Otherwise} \end{cases} \tag{49}$$

where x_m and x_n denote the waveforms transmitted at the mth and nth transmitters, respectively.

The use of STSOW will remove the effects of the receive beams sidelobes overlapping with the next adjacent mainlobes. The AASR will therefore be improved.

IV. Simulation Results

The following section shows the numerical results of our proposed MIMO-SAR configuration using an LFM waveform and compares it with a conventional MIMO-SAR. In addition, it compares the point spread function (PSF) of the proposed FDSI-based estimation algorithm with the one obtained using the MF.

A. Range Profile Estimation Performance

The PSF of the proposed FDSI-based estimation algorithm is compared with the one obtained using the MF as shown in Fig. 6. It is assumed in the simulation that the waveform used is a conventional LFM with a bandwidth of 100 MHz. It is clear in Fig. 6 that the proposed FDSI-based algorithm exhibits the IRCI-free property because the nonflat spectrum of the LFM waveform is considered which makes the range profile estimation performance better than the one obtained using the MF (i.e., which assumes a flat spectrum).

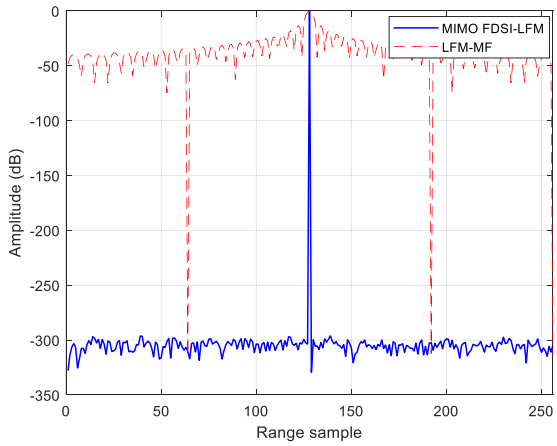

Fig. 6. Normalized PSF of the FDSI-based algorithm and LFM-MF method.

B. 1-D Echo Separation

Consider a scenario in which there are $M = 3$ transmit antennas, $N = 3$ receive antennas as shown in Fig. 1, the number of elevation channels is $N_{\text{el}} = 25$ and the channel impulse response length is $L = 4268$. The transmitted waveform is an LFM waveform with a bandwidth of 100 MHz and the sampling frequency is $F_s = 200$ MHz. The SNR in the simulation is assumed to be 40 dB and the timing diagram of the transmission is as shown in Fig. 2. Assume that there are three scatterers separated by a delay difference is $t_d = 3\,\mu$s which is the same as the pulsewidth. This scenario (i.e., in which only the range dimension is considered) is presented to demonstrate how the received signals that correspond to different phase centers are separated at the receiver using DBF in elevation.

The received signal before and after estimating the impulse response at the first receiver is shown in Fig. 7(a) and (b), respectively, where one can see that the impulse responses corresponding to different phase centers are overlapped. The separation is possible because echoes corresponding to different subpulses (at each instant of time) arrive from different elevation angles. The separated impulse responses without delay compensation whose phase centers are located at the center of Tx1/Rx1, at the center of Tx2/Rx2 and midway between Tx1/Rx1 and Tx2/Rx2 are shown in Fig. 7(c)–(e), respectively.

C. Azimuth Ambiguity Removal

Consider the simulation parameters listed in Table I and assume that there are two adjacent scatterers located at the swath center. The transmitted waveform is an LFM waveform with bandwidth of 100 MHz and the timing diagram of the transmission is as shown in Fig. 2. The azimuth and range cuts for the noiseless case are as shown in Figs. 8 and 9, respectively. It is clear from Fig. 8 that there is no azimuth aliasing using our proposed MIMO configuration even though the PRF used is $B_d/(MN) = B_d/9 \approx 34$ Hz unlike the case of the conventional MIMO SAR in which minimum PRF should satisfy the inequality $\text{PRF}_{\text{min}} \geq (B_d/K_p = B_d/5)$ where K_p is the number

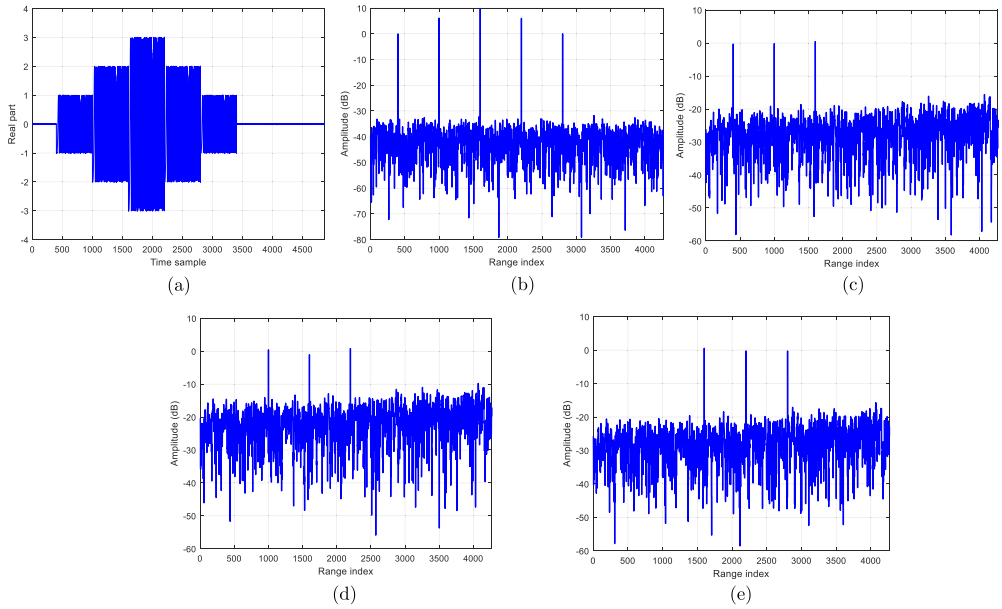

Fig. 7. 1-D echo separation. (a) Real part of the received signal. (b) Estimated impulse response before DBF in elevation. (c) Separated impulse response whose phase center is located at the center of Tx1/Rx1. (d) Separated impulse response whose phase center is located at the center of Tx2/Rx2. (e) Separated impulse response whose phase center is located midway between Tx1/Rx1 and Tx2/Rx2.

TABLE I
SIMULATION PARAMETERS

Parameter	Symbol	Value
Number of Tx (Rx)	$M\ (N)$	3
Min. distance to the swath centre	R_0	$20km$
Look angle	ϕ	45^o
Azimuth length of the conventional MIMO SAR beamformer	L_a	$1.5m$
Azimuth length of the proposed MIMO SAR beamformer	$L_{a,\text{prop}}$	$4.5m$
Distance between adjacent Tx/Rx in (proposed) MIMO SAR	$(d_{\text{prop}})\ d$	$(4.5m)\ 1.5m$
Doppler bandwidth	B_d	$300Hz$
Pulse repetition frequency	f_p	$34Hz$
Platform Velocity	v_p	$225m/s$
Carrier Frequency	F_c	$4.5GHz$
Sampling Frequency	F_s	$200MS/s$
Single waveform Bandwidth	BW	$100MHz$
Number of elevation channels	N_{el}	20
Pulse width	τ	$2.5\mu s$

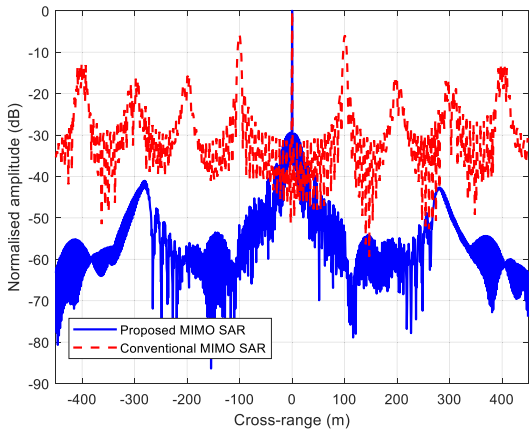

Fig. 8. Azimuth cut of a scatterer in the estimated scene using the proposed and conventional MIMO SAR.

of independent phase centers which is equal to $(M + N - 1)$ when the same antenna arrays are used for both transmission and reception. Accordingly, our proposed MIMO configuration outperforms the conventional MIMO-SAR. It should be noted that it has been assumed that the waveforms used in the conventional MIMO-SAR are perfectly orthogonal.

D. Azimuth Ambiguity to Signal Ratio

In this section, the simulation of the azimuth ambiguity characteristics of the proposed MIMO-SAR configuration is performed and compared with the azimuth ambiguity characteristics of the conventional SISO SAR using an AASR criterion. Consider the beam patterns of the transmitters and receivers of the proposed MIMO-SAR and conventional SISO SAR shown in Fig. 10. The 3 dB width of the beam pattern of the conventional SISO SAR has been chosen in such a way that both of proposed MIMO-SAR and conventional SISO SAR have the same cross-range resolution.

The AASR of the proposed MIMO SAR configuration with and without the use of STSOW is illustrated in Fig. 11(a) as a function of PRF. The PRF in Fig. 11(a) starts from 100˜Hz because it corresponds to the 3 dB Doppler bandwidth of one individual narrow receiving beam (i.e., it is assumed that the aliasing of the Doppler spectrum of the individual narrow beams has been removed using the multiaperture reconstruction algorithm described previously). The AASR of the conventional SISO SAR is shown in Fig. 11(b). One can see that the AASR in Fig. 11(a) of the side beam is worse than that of the central beam because the power of desired signal component [i.e., second term of (48)] is lower than that of the central beam for the case when

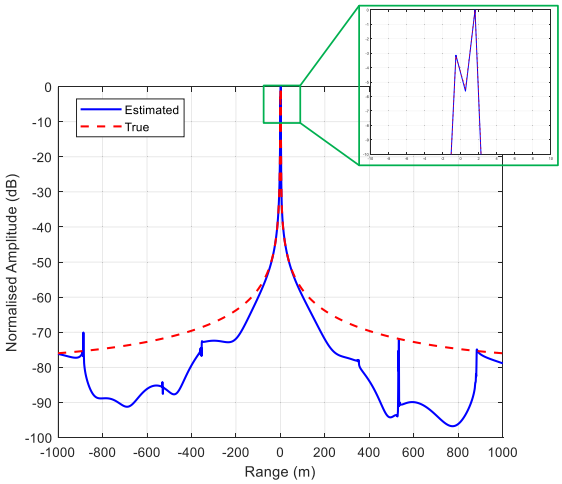

Fig. 9. Range cut of the true and estimated scene.

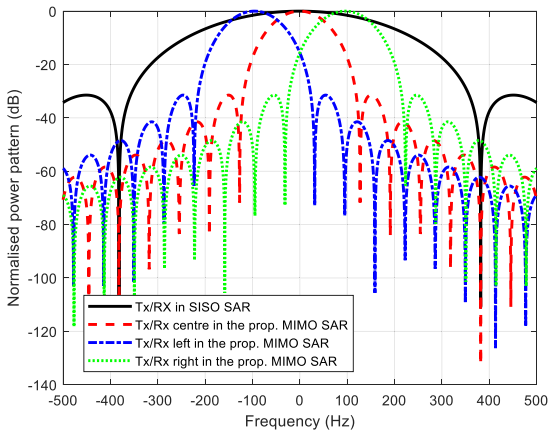

Fig. 10. Transmit and receive beam patterns of the proposed MIMO-SAR and conventional SISO SAR as a function of frequency.

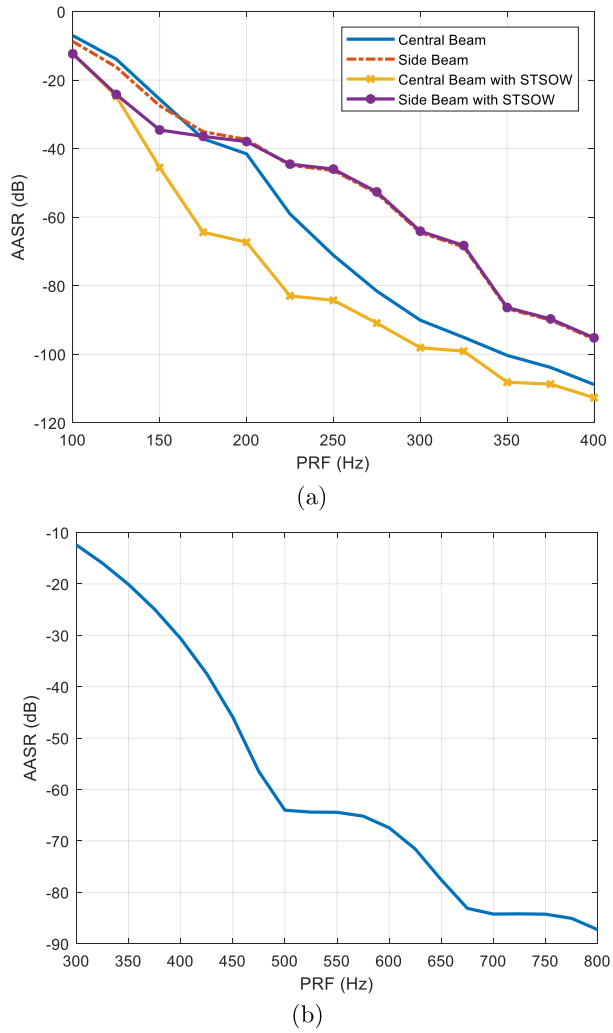

Fig. 11. Azimuth ambiguity characteristics. (a) Proposed MIMO-SAR with and without STSOW. (b) Conventional SISO SAR.

the same waveforms are used for transmission. In addition, the AASR of the central beam for the case of STSOW is the same as the one in the conventional SISO SAR [i.e., the second terms of (47) and (48) are zero].

E. Raw Data Simulation

MIMO SAR data are constructed as explained in [7] and [28] using a publicly available airborne SISO SAR data "Gotcha" [29] to validate the proposed configuration in a cluttered scene.

It is assumed, for the sake of simplicity, that echoes correspond to each transmitter have been already separated at the receiver using DBF in elevation on receive as explained previously. In addition, the waveforms used in the conventional MIMO SAR are assumed to be perfectly orthogonal. The MIMO SAR data are down-sampled such that the effective sampling frequency in the azimuth dimension is $1/10$ of the Nyquist frequency.

Consider the main system parameters listed in Table II. The formed images using a single receiver and all receivers of the proposed MIMO SAR configuration are shown in Figs. 12 and 13, respectively. It is clear from the figure that the formed image using all the receivers has a better cross-range resolution than that of the formed image using a single receiver because only a portion of the Doppler bandwidth is utilized in the single receiver image.

TABLE II
SYSTEM PARAMETERS

Parameter	Symbol	Value
Number of Tx (Rx)	$M(N)$	3
Min. distance to the swath centre	R_0	$10.158km$
3dB width of a single receiver beamwidth in the proposed MIMO	θ_{BW}	2^o
3dB width of a single receiver beamwidth in the conventional MIMO	$\theta_{BW,\text{conv}}$	6^o
Distance between adjacent Tx/RX in the proposed MIMO	d	$4.5m$
Distance between adjacent Tx/RX in the conventional MIMO	d_{conv}	$1.5m$
Carrier Frequency	F_c	$9.58GHz$
Single waveform Bandwidth	BW	$600MHz$

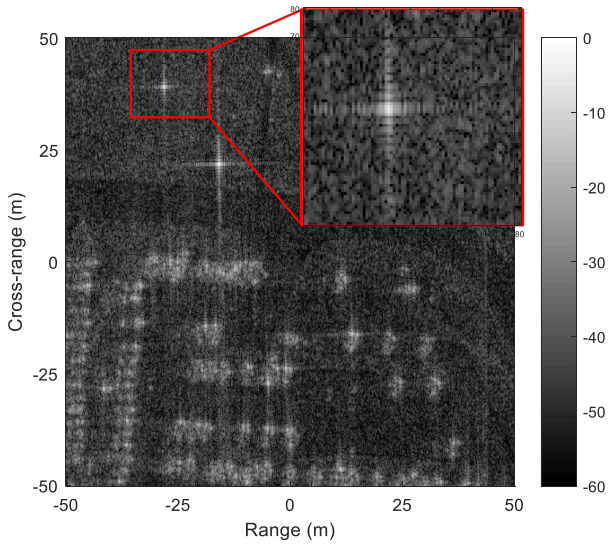

Fig. 12. Formed image using a single received data.

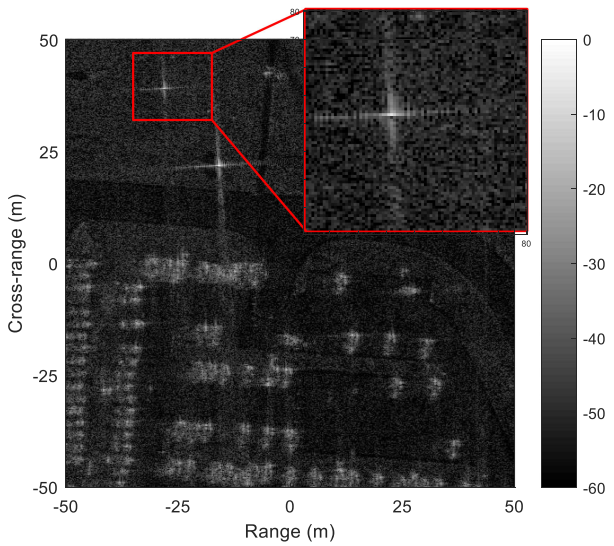

Fig. 13. Formed image using all received data in the proposed MIMO-SAR.

Next, The proposed MIMO-SAR configuration will be compared with the conventional MIMO-SAR. Assume that the sampling frequency of the conventional MIMO-SAR across the azimuth dimension is the same as the one used in the proposed MIMO-SAR configuration. The formed image of the conventional MIMO-SAR is shown in Fig. 14. It is clear from this figure that the image is aliased.

The cross-range cuts of the indicated areas with red rectangles in the formed images depicted in Figs. 12 and 13 is shown in Fig. 15 where one can see that the formed image using all the receivers has a better cross-range resolution than that of the formed image using a single receiver because only a portion of the Doppler bandwidth is utilized in the single receiver image.

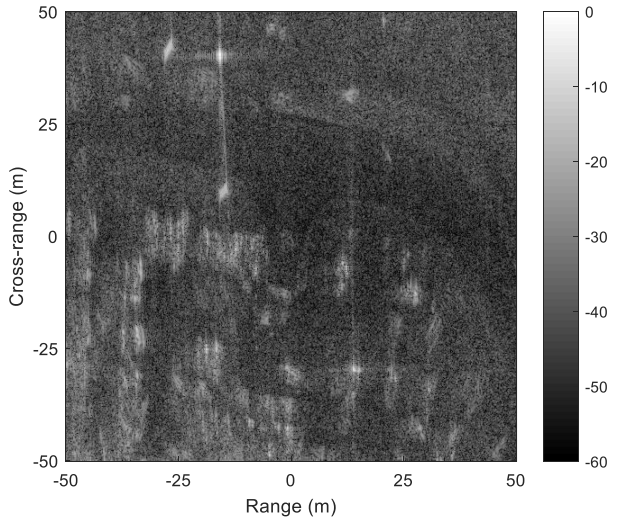

Fig. 14. Formed image using conventional MIMO-SAR in which the azimuth sampling frequency is the same as the one used in the proposed MIMO-SAR.

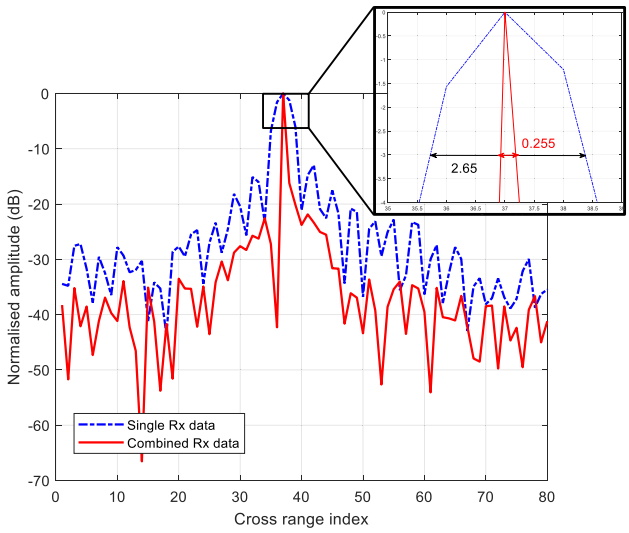

Fig. 15. Cross-range cuts of the indicated area with red rectangles in Figs. 12 and 13.

V. Conclusion

In this article, a new MIMO-SAR configuration with multiple contiguous azimuth beams is proposed to obtain high-resolution wide swath imaging. The proposed configuration utilizes all the phase centers including the overlapping ones which allows to use a lower operating PRF as compared with the conventional MIMO-SAR. It is due to the multiple contiguous azimuth beams which makes the echoes, whose effective phase centers are overlapped, occupy different Doppler bandwidths. The waveforms used for transmission consists of a sequence of LFM waveforms which share the same bandwidth and have the same cener frequency. The estimated range profile is free from IRCI which is a result of using an FDSI-based estimation algorithm instead of MFs. Echoes corresponding to different phase centers are separated at the receiver using DBF on receive in elevation. Finally,

simulation results of point targets and constructed raw data are used to validate the efficiency of the proposed configuration.

REFERENCES

[1] G. Krieger, N. Gebert, and A. Moreira, "Hochauösendes synthetik-apertur-seitensicht-radarsystem mittels digital beamforming." *German Patent Application DE*, vol. 10, p. 022, 2006.

[2] G. Min, W. Xiaoming, and H. Shunji, "Performance improvements in MIMO SAR," in *Proc. IEEE Radar Conf.*, Rome, 2008, pp. 1–3, doi: 10.1109/RADAR.2008.4720969.

[3] J. H. G. Ender and J. Klare, "System architectures and algorithms for radar imaging by MIMO-SAR," in *Proc. IEEE Nat. Radar Conf.*, Pasadena, CA, USA, 2009, pp. 1–6, doi: 10.1109/RADAR.2009.4976997.

[4] W. Q. Wang, "Space-time coding MIMO-OFDM SAR for high-resolution imaging," *IEEE Trans. Geosci. Remote Sens.*, vol. 49, no. 8, pp. 3094–3104 Aug. 2011.

[5] W. Xu, Y. Deng, and R. Wang, "Multichannel synthetic aperture radar systems with a planar antenna for future spaceborne microwave remote sensing," *IEEE Aerosp. Electron. Syst. Mag.*, vol. 27, no. 12, pp. 26–30, Dec. 2012.

[6] W. Xu, P. P Huang, and Y.-K. Deng, "MIMO-TOPS mode for high-resolution ultra-wide-swath full polarimetric imaging," *Prog. Electromagn. Res.*, vol. 121, pp. 19–37, 2011.

[7] M. Alshaya, M. Yaghoobi, and B. Mulgrew, "High-resolution wide-swath IRCI-free MIMO SAR," *IEEE Trans. Geosci. Remote Sens.*, vol. 58, no. 1, pp. 713–725 Jan. 2020.

[8] X. Luo, R. Wang, Y. Deng, and W. Xu, "Influences of channel errors and interference on the OFDM-MIMO SAR," in *Proc. IEEE Radar Conf.*, 2013, pp. 1–5.

[9] G. Jing, G. Sun, X. Xia, M. Xing, and Z. Bao, "A novel two-step approach of error estimation for stepped-frequency MIMO-SAR," *IEEE Geosci. Remote Sens. Lett.*, vol. 14, no. 12, pp. 2290–2294 Dec. 2017.

[10] G. Krieger, "MIMO-SAR: Opportunities and pitfalls," *IEEE Trans. Geosci. Remote Sens.*, vol. 52, no. 5, pp. 2628–2645 May 2014.

[11] G. Krieger *et al.*, "MIMO-SAR and the orthogonality confusion," in *Proc. Int. Geosci. Remote Sens. Symp.*, Munich, Gremany, 2012, pp. 1533–1536, doi: 10.1109/IGARSS.2012.6351242.

[12] W. Q. Wang, "Mitigating range ambiguities in high-PRF SAR with OFDM waveform diversity," *IEEE Geosci. Remote Sens. Lett.*, vol. 10, no. 1, pp. 101–105 Jan. 2013.

[13] W. Q. Wang and J. Cai, "Ground moving target indication by MIMO SAR with multi-antenna in azimuth," in *Proc. Int. Geosci. Remote Sens. Symp.*, 2011, pp. 1662–1665.

[14] H. Sun, F. Brigui, and M. Lesturgie, "Analysis and comparison of MIMO radar waveforms," in *Proc. Int. Radar Conf.*, Lille, France, 2014, pp. 1–6, doi: 10.1109/RADAR.2014.7060251.

[15] J. P. Stralka, R. M. Thompson, J. Scanlan, and A. Jones, "MISO radar beamforming demonstration," in *Proc. RadarCon RADAR*, Kansas City, MO, USA, 2011, pp. 889–894, doi: 10.1109/RADAR.2011.5960665.

[16] P. P. Vaidyanathan and P. Pal, "MIMO radar, SIMO radar, and IFIR radar: A comparison," in *Proc. Conf. Rec. Asilomar Conf. Signals, Syst. Comput.*, Pacific Grove, CA, USA, 2009, pp. 160–167, doi: 10.1109/ACSSC.2009.5470139.

[17] Y. H. Cao and X. G. Xia, "IRCI-Free MIMO-OFDM SAR using circularly shifted Zadoff–Chu sequences," *IEEE Geosci. Remote Sens. Lett,*, vol. 12, no. 5, pp. 1126–1130, Jan. 2015.

[18] G. Krieger, N. Gebert, and A. Moreira, "Multidimensional waveform encoding: A new digital beamforming technique for synthetic aperture radar remote sensing," *IEEE Trans. Geosci. Remote Sens.*, vol. 46, no. 1, pp. 31–46, Jan. 2008.

[19] W. Wang, R. Wang, Y. Deng, L. Hou, W. Xu, and L. Guo, "A processing scheme for LFM-based waveform MIMO SAR with digital beam-forming in elevation," *Remote Sens. Lett.*, vol. 6, no. 11, pp. 874–883 2015. [Online]. Available: https://doi.org/10.1080/2150704X.2015.1088672

[20] M. Alshaya, M. Yaghoobi, and B. Mulgrew, "Resolution enhancement in high resolution wide swath MIMO SAR," in *Proc. IEEE Int. Radar Conf.*, Washington, DC, USA, 2020, pp. 339–344, doi: 10.1109/RADAR42522.2020.9114563.

[21] W. Xu, P. P. Huang, and Y.-K. Deng, "Multi-channel SPCMB-tops SAR for high-resolution wide-swath imaging," *Prog. Electromagn. Res.*, vol. 116, pp. 533–551, 2011.

[22] N. Gebert, G. Krieger, and A. Moreira, "Multichannel azimuth processing in ScanSAR and TOPS mode operation," *IEEE Trans. Geosci. Remote Sens.*, vol. 48, no. 7, pp. 2994–3008, Jul. 2010.

[23] M. Suess, B. Grafmueller, and R. Zahn, "A novel high resolution, wide swath SAR system," in *Proc. Scanning Present Resolving Future. Proc. IEEE Int. Geosci. Remote Sens. Symp.*, Sydney, NSW, Australia, 2001, vol. 3, pp. 1013–1015, doi: 10.1109/IGARSS.2001.976731.

[24] W. Xu, W. Xu, and Y. Deng, "Multichannel SAR with reflector antenna for high-resolution wide-swath imaging," *IEEE Antennas Wireless Propag. Lett.*, vol. 9, pp. 1123–1126, 2010.

[25] Harry L. Van Trees, *Optimum Array Processing: Part IV of Detection, Estimation, and Modulation Theory*. New York, NY, USA: Wiley, 2002.

[26] M. AlShaya, M. Yaghoobi, and B. Mulgrew, "Frequency domain system identification for wide swath high resolution IRCI-free MIMO SAR," in *Proc. IEEE Radar Conf.*, 2019, doi: 10.1109/RADAR.2019.8835622.

[27] R. Bamler, "A comparison of range-Doppler and wavenumber domain SAR focusing algorithms," *IEEE Trans. on Geosci. Remote Sens.*, vol. 30, no. 4, pp. 706–713, Jul. 1992.

[28] M. Xing, Z. Bao, F. Zhou, J. Zhang, and G. Sun, "An efficient signal reconstruction algorithm for stepped frequency MIMO-SAR in the spotlight and sliding spotlight modes," *Int. J. Antennas Propag.*, vol. 2014, 2014, Art. no. 329340.

[29] "Gotcha volumetric SAR data set, Version 1.0," [Online]. Available: https://www.sdms.afrl.af.mil/

Mohammed AlShaya (Graduate Student Member, IEEE) received the B.Eng. degree (Hons.) in electrical engineering (communications and electronics) from King Saud University, Riyadh, Saudi Arabia, in 2011 and the M.Sc. degree in communications and signal processing with distinction from Imperial College London, London, U.K., in 2015. He is currently working toward the Ph.D. degree in digital communications with the Institute of Digital Communications, University of Edinburgh, Edinburgh, U.K.

He then worked as an Academic Researcher with King Abdulaziz City for Science and Technology, where he was involved in many radar development projects. His research interests include adaptive array signal processing, compressive sensing, and MIMO radar. He is a Chartered Engineer.

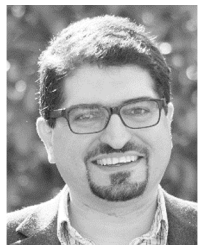

Mehrdad Yaghoobi (Member, IEEE) received the Ph.D. degree in signal processing from the University of Edinburgh, Edinburgh, U.K., in 2010.

He is an Assistant Professor with the University of Edinburgh in signal processing and machine learning. He worked as a Postdoctoral Researcher until 2016. He has authored more than 40 conferences and journal articles and some of his developed algorithms have already been commercialized. His research interests include sparse and low-dimensional signal modeling, machine learning, and computationally low-cost algorithms, suitable for edge computing.

Bernard (Bernie) Mulgrew (Fellow, IEEE) received the B.Sc. degree from Queen's University Belfast, Belfast, U.K, in 1979 and the Ph.D. degree from University of Edinburgh, Edinburgh, U.K., in 1987.

After graduation, he worked for four years as a Development Engineer with the Radar Systems Department, Ferranti, Edinburgh. From 1983 to 1986, he was a Research Associate with the Department of Electrical Engineering, University of Edinburgh. He was appointed to lectureship, in 1986, promoted to Senior Lecturer, in 1994 and became a Reader, in 1996. The University of Edinburgh appointed him as a Personal Chair. in October 1999 (Professor of Signals and Systems). He has co-author of three books on signal processing. His research interests include adaptive signal processing and estimation theory and in their application to radar and sensor systems.

Dr. Mulgrew is a fellow of Royal Academy of Engineering, Royal Society of Edinburgh, and Institution of Engineering and Technology.